Saudi Pharmaceutical Journal 28 (2020) 15–24

Contents lists available at ScienceDirect

Saudi Pharmaceutical Journal

journal homepage: www.sciencedirect.com

Original article

Synthesis and characterization of mesoporous SBA-15 and SBA-16 as carriers to improve albendazole dissolution rate

María Esperanza Adrover [b,c], Marisa Pedernera [b,c], Magali Bonne [d,e], Bénédicte Lebeau [d,e], Verónica Bucalá [b,c], Loreana Gallo [a,c,*]

[a] Departamento de Biología, Bioquímica y Farmacia, Universidad Nacional del Sur (UNS), San Juan 670, 8000 Bahía Blanca, Argentina
[b] Departamento de Ingeniería Química, Universidad Nacional del Sur (UNS), Av. Alem 1253, 8000 Bahía Blanca, Argentina
[c] Planta Piloto de Ingeniería Química, PLAPIQUI (UNS-CONICET), Camino La Carrindanga Km 7, 8000 Bahía Blanca, Argentina
[d] Université de Haute Alsace (UHA), CNRS, IS2M UMR 7361, 68100 Mulhouse, France
[e] Université de Strasbourg, 67000 Strasbourg, France

ARTICLE INFO

Article history:
Received 22 August 2019
Accepted 2 November 2019
Available online 13 November 2019

Keywords:
Albendazole
Mesoporous materials
Drug loading
Solubility
Dissolution rate

ABSTRACT

Albendazole (ABZ, anti-parasitic active pharmaceutical ingredient) is a crystalline low water-soluble drug, thus the dissolution rate in gastrointestinal fluids is limited. Consequently, the improvement of the water solubility and dissolution rate of ABZ implies a great challenge for a more efficient treatment of hydatidosis. In this context, SBA-15 and SBA-16 ordered mesoporous silica materials were synthetized and loaded with ABZ. X-ray diffraction, FT-IR spectroscopy, nitrogen physisorption manometry, particle size distribution and scanning electronic microscopy were used to characterize unloaded and loaded materials (ABZ/SBA-15 and ABZ/SBA-16). The loaded ABZ amount in the carriers was estimated by elemental analysis. For the loaded materials, the drug solubility and release profile were evaluated. In addition, mathematical models were compared to explain the dissolution kinetics of ABZ from mesoporous solids. ABZ was successfully loaded into the mesopores. The amorphous state of the adsorbed ABZ was confirmed by differential scanning calorimetry that resulted in a notable increment in the dissolution rate compared to crystalline ABZ. Drug release behaviors were well simulated by the Weibull model for ABZ/SBA-15 and by the Gompertz function for pure ABZ and ABZ/SBA-16. The SBA-15 carrier exhibited the highest drug loading and dissolution rate becoming a promising material to improve ABZ bioavailability.

1. Introduction

Human echinococcosis is a parasitic infection produced by tapeworms of the genus *Echinococcus*. This parasite attacks canines, which house the adult worm in the intestine. When sheep or cattle ingest contaminated canine feces, they become the intermediate hosts and if canines consume lamb or beef containing the larvae the cycle is completed. Persons can be infected due to the ingestion of food, soil and water contaminated with parasite eggs or by direct contact with animal hosts. The disease can be presented mainly in two forms: cystic echinococcosis (hydatidosis) and alveolar echinococcosis caused by *Echinococcus granulosus and E. multilocularis*, respectively. These two forms are of medical and public health relevance, especially in endemic regions (Argentina, Peru, East Africa, Central Asia and China) where human incidence rates for cystic echinococcosis are 50 per 100.000 person-years, and prevalence levels higher than 10%. In the year 2015, the World Health Organization (WHO) estimated that echinococcosis produces 19.300 deaths and about 871.000 disability-adjusted life-years globally each year. Annual costs associated with this disease are estimated to be US$ 3 billion for treating cases and losses to the livestock industry (WHO, 2019).

Hydatidosis is characterized by the presence of one or more hydatid cysts (i.e., slow growing fluid-filled structures that contain the larvae) located mainly in the liver and lungs. There are four main ways to treat this disease: medication, percutaneous treatment, surgery, and the watch and wait method for non-active cysts

* Corresponding author at: Departamento de Biología, Bioquímica y Farmacia, Universidad Nacional del Sur (UNS), San Juan 670, 8000 Bahía Blanca, Argentina. PLAPIQUI (UNS-CONICET), Camino La Carrindanga Km 7, 8000, Bahía Blanca, Argentina.
E-mail address: lgallo@plapiqui.edu.ar (L. Gallo).
Peer review under responsibility of King Saud University.

Production and hosting by Elsevier

https://doi.org/10.1016/j.jsps.2019.11.002
1319-0164/

(Brunetti and Junghanss, 2009). Antiparasitic drugs (benzoimidazole carbamates) constitute the better option in non-complex cysts or cysts located in non-vital parts of the body, and in persons in which surgery is hazardous. Also, medicine treatment decreases the danger of recurrence when is used previously or after surgery and percutaneous treatments (Anadol et al., 2001). Several investigators and clinicians consider Albendazole (ABZ) the drug of choice to treat hydatidosis. The drug dosage is of 15 mg/kg/day (400 mg tablets, two daily intakes) for 3–6 months (Falagas and Bliziotis, 2007; Stamatakos et al., 2009). Recently, Fattahi Masoom et al. (2017) reported a study of the efficacy of ABZ administered for a long period of time (six months divided in three 8-week stages, each stage comprising of six weeks treatment followed by two weeks without medication). The cure rate in persons who finished one, two, and three stages were 7.5%, 21.7% and 66.1%, respectively. Thus, the administration scheme evaluated, which comprises stages of no treatment, seems to produce better results in comparison to the continuous treatment. As it can be seen, the treatment with ABZ implies a high dose and long period of treatment. These inconveniences may be mainly associated to the low water solubility of the drug (0.2 μg/mL at 25 °C) that limits the dissolution rate in the gastrointestinal fluids. Consequently, the drug absorption rate is poor and erratic, producing low drug levels in plasma (Pensel et al., 2015, 2014). Therefore, the increment of the aqueous solubility and dissolution rate of ABZ implies a great challenge to achieve a more efficient treatment of hydatidosis. In this sense, different technologies were used to increase the solubility/dissolution rate of ABZ, such as: (i) solid dispersions (Castro et al., 2010; Jiménez de los Santos et al., 2017; Kohri et al., 1999; Martinez-Marcos et al., 2016), (ii) complexation with β-cyclodextrins (Chattah et al., 2017; Evrard et al., 2002; García et al., 2014; Palomares-Alonso et al., 2010) and acyclic cucurbit [n]uril molecular containers (Ma et al., 2012), (iii) co-griding with various excipients by jet-mill (Vogt et al., 2008), (iv) extrusion/spheronization (Ibrahim and Al-Anazi, 2013), (v) emulsification/solvent evaporation methods (Abulaihaiti et al., 2015; Souza and Marchetti, 2012), (vi) spray-drying (García et al., 2013b, 2013a; Ibrahim et al., 2014; Priotti et al., 2017), vii) high pressure homogenization combined with spray-drying (Paredes et al., 2016), (viii) solvent recrystallization and spherical agglomeration (Thakur et al., 2015), (ix) encapsulation in liposomes (Haitao et al., 2016; Li et al., 2015; Panwar et al., 2010) and (x) nanoformulations (Movahedi et al., 2017). In general, these techniques require numerous production stages, several materials and organics solvents. A more direct technique than the previously mentioned is to load low water-soluble drug into different types of carriers, e.g., micelles (Panja et al., 2016), mesoporous silica nanoparticles (Abbaraju, 2017; Jambhrunkar et al., 2013; Lu et al., 2007), and polymer-modified inorganic nanoparticles (Panja et al., 2015; Panja et al., 2016). To the best of our knowledge, the strategy to direct load ABZ into ordered mesoporous silica materials in order to enhance the solubility/dissolution rate of the drug has not been previously investigated. Ordered mesoporous silica particles are nontoxic and biocompatible materials and have several attractive characteristics to improve drug dissolution, such as: high surface area, large pore volume, and long-range ordered pore structure. In addition, these carriers show higher resistance to heat, pH and stability on storage in comparison to many polymers commonly used to enhance drug solubility. The porous structure of ordered mesoporous silica materials permit the confinement and stabilization of drug molecules within the pores in an amorphous state that improves the drug solubility/dissolution rate in comparison to the crystalline state (Li et al., 2012; Mccarthy et al., 2015). In this sense, the ordered mesoporous silica particles SBA-15 and SBA-16 are promising materials for improving drug delivery due to their dual-porosity system. This means that SBA materials present micropores interconnecting mesopores endowing them with thermal and hydrothermal stability. SBA-15 has hexagonal pores in a 2D array while SBA-16 presents a 3D body-centered cubic arrangement (Stevens et al., 2006) (Hu et al., 2012). As summarized in the review reported by Xu et al. (2013) (Xu et al., 2013), SBA-15 was proposed as a carrier of different low water-soluble drugs, (e.g., ezetimibe, fenofibrate, glibenclamide, ibuprofen, indomethacin, itraconazole, telmisartan and griseofulvin). Additionally, *in-vivo* studies of poor-water soluble drugs such as carbamazepine, fenofibrate and ketoprofen with SBA-15 as carrier were reported (Riikonen et al., 2018). On the other hand, there is a lower number of studies focusing on SBA-16 as carrier for hydrophobic drugs (Zhang and Cresswell, 2016). Thomas et al. (2010) (Thomas et al., 2010) produced SBA-16 for loading antiepileptic drugs (oxcarbazepine, rufinamide and carbamazepine). The incorporation of these drugs within the mesoporous solids leads to an effective particle size decrease improving dissolution rates. Hu et al. (2011) (Hu et al., 2011) studied the SBA-16 material for the delivery of the non-steroidal anti-inflammatory agent indomethacin (water-insoluble drug). The drug exhibited a marked enhancement in the dissolution rate after being loaded into the silica particles. In addition, Hu et al. (2012) (Hu et al., 2012) compared the dissolution profiles for carvedilol loaded into 3D cubic SBA-16 and 2D hexagonal MCM-41 (mesoporous material), displaying for SBA-16 a more fast release in comparison with MCM-41.

In this context, the novelty of this work was to load ABZ into ordered mesoporous silica materials in order to augment the solubility/dissolution rate of the drug. For this purpose, the materials SBA-15 and SBA-16 were synthetized and loaded with ABZ by the immersion method in order to compare their behavior as a platform for bioapplication. X-ray diffraction and scanning electronic microscopy were employed to characterize SBA-15 and SBA-16. FT-IR, nitrogen sorptometry and thermogravimetry–differential scanning calorimetry were carried out to compare the synthesized unloaded (SBA-15 and SBA-16) and the loaded materials (ABZ/SBA-15 and ABZ/SBA-16). The amount of ABZ loaded in the carriers was estimated by elemental analysis. For the loaded materials the drug solubility and release profile were evaluated. In addition, mathematical models were compared to describe the dissolution kinetics of ABZ from mesoporous silica materials.

2. Experimental section

2.1. Materials

Tetraethyl orthosilicate (TEOS), Pluronic P123, Pluronic F127 were obtained from Sigma Aldrich (Germany). The solvents butanol, acetic acid, hydrochloric acid were purchased from Anedra (Argentina) and crystalline albendazole from Parafarm (98.52% purity) (Argentina). The spectroscopic grade potassium bromide was obtained from Merck (Germany). All reagents were of analytical grade and were employed as received from the supplier.

2.2. Synthesis of ordered mesoporous silica carriers: SBA-15 and SBA-16

The synthesis of the SBA-15 silica material was realized according to the protocol proposed by Zhao et al. (1998) (Zhao et al., 1998) and modified by Belmoujahid et al. (2015) (Belmoujahid et al., 2015). First, Pluronic P123 was dissolved in hydrochloric solution at 40 °C. After total dissolution TEOS was added, the medium was kept at 40 °C and stirred for 2 h. The composition of the obtained gel was: 1 TEOS: 0.017 P123: 5.68 HCl: 197 H_2O. The hydrothermal synthesis was carried out for 24 h in an oven at 90 °C in a sealed polypropylene bottle. The solid material was

recovered by Büchner filtration, washed with distilled water and dried overnight in an oven at 70 °C. The solid was then calcined in a muffle furnace at 300 °C under air for 4 h with a heating rate of 1 °C/min.

SBA-16 was synthesized following the procedure reported by Gobin et al. (2007) (Gobin et al., 2007) with a gel composition of: 1 TEOS: 0.003 F127: 0.8 HCl: 1.8 C_4H_9OH: 120 H_2O. Pluronic F127 was dissolved in hydrochloric solution. After 30 min of agitation, butanol was added as co-surfactant. Next, TEOS was added and stirred during 24 h at ambient temperature (25 °C). The mixture was poured into a Teflon autoclave and heated for 48 h in an oven at 60 °C. Finally, the material was washed with tri-distillated water by means of three 30 min centrifugation cycles (at 5000 rpm). Subsequently, the synthesized material was dried in an oven at 70 °C for one night. The obtained solid was calcined for 6 h in a muffle furnace at 500 °C for 6 h with a heating rate of 2 °C/min.

2.3. Drug loading procedure

The immersion method was used to load ABZ onto the SBA-15 and SBA-16. To this end, 1250 mg of ABZ was dissolved in 25 mL of acetic acid up to completely dissolution. Then, 419 mg of ordered mesoporous silica particles were added. The sample was kept under stirring for 48 h at ambient temperature (25 °C). Subsequently, the sample was centrifuged for 30 min at 8000 rpm to separate the supernatant from the precipitated solid (ABZ/SBA-15 and ABZ/SBA-16). Firstly, the materials were dried at room temperature for 72 h. Then, the solids were heated at 60 °C using a moisture analyzer with halogen heating (model M45, Ohaus, Pine Brook, USA) until constant weight was reached.

2.4. Powder X-ray diffraction

The pore structure of the materials was determined by X-ray diffraction in a Bruker D2 Phaser device using CuK radiation (λ = 1.54 Å) with a Ni filter, with step 0.01°, with divergent slots and convergent 0.1 mm and 3 mm respectively, 10 mA current, the 30 kV voltage using a LYNXEYE detector.

2.5. Scanning electron microscopy and particle size distribution

The morphology of SBA-15 and SBA-16 was assayed by a scanning electron microscopy (SEM, JEOL 35CF) with an acceleration potential of 10 kV. The samples were dried under air flow on a porthole and posteriorly were metalized with gold coating (thickness of 245 Å) (PELCO 91,000 sputter coater). A transmission electron microscopy (TEM, JEOL, 100 CX) with an acceleration potential of 100 kV was employed. The samples were prepared by dispersing the powder in an ethanol solution and placed in an ultrasonic bath for 15 min. Then, few drops were placed on a holey carbon film on 200 mesh grids.

Both SEM and TEM digitized images were processed by means of Fiji software in order to measure the particle maximum Feret diameter (i.e., the longest dimension of the particle).

2.6. Fourier transform infrared (FTIR) spectroscopy

The chemical identity of pure materials (SBA-15, SBA-16, ABZ) and the loaded ones (ABZ/SBA-15 and ABZ/SBA-16) was verified by diffuse reflectance infrared Fourier transform spectroscopy (DRIFTS, Nicolet 6700FT-IR spectrometer). The samples were mixed with KBr and the IR spectra (average scans = 64, resolution = 4 cm^{-1}) were obtained between 400 and 4000 cm^{-1}.

2.7. Nitrogen physisorption manometry analysis

The specific surface area of the materials was analyzed by N_2 adsorption–desorption isotherms at 77 K by means of the Brunauer-Emmet-Teller method (BET) multipoint method P/P_0 values between 0.05 and 0.35. The analysis was carried out in the Autosorb iQ gas sorption analyzer (Quantachrome Instruments). Prior to analysis, SBA-15 and SBA-16 were degassed and dried at 200 °C for 7 h, while ABZ/SBA-15 and ABZ/SBA-16 were degassed and dried at 60 °C for 24 h. The pore size distributions (PSDs) were obtained using the Barrett-Joyner-Halenda (BJH) model. (Sapag, 2011).

The microporous volume and the microporous surface area were determined using the Harkins and Jura *t-plot* (Galarneau et al., 2014).

2.8. Elemental analysis

The loading efficiency of ABZ in SBA-15 and SBA-16 was evaluated by elemental analysis (C, H, and N) employing an Exeter Analytical CE-440 apparatus (Exeter Analytical). The weights of the samples ranged between 1.59 and 1.64 mg.

2.9. Differential scanning calorimetry

The physical state of the pure drug and the loaded mesoporous silica samples were examined by differential scanning calorimetry (DSC) (Pyris 1, Perkin Elmer). The thermographs of each sample were performed under continuous flow of N_2 (10 mL/min) and a temperature ramp of 10 °C/min from a temperature of 25 °C up to 260 °C.

2.10. Solubility studies

Three stoppered flasks with 2 mg/mL of ABZ (concentration 25 times higher than the reported drug solubility in 5 mL HCl 0.1 N solutions at 37 °C) were used for pure ABZ (Elsamaligy, 2014). Likewise, an equivalent amount of drug content for ABZ/SBA-15 and ABZ/SBA-16 were employed to evaluate ABZ solubility from the loaded materials. These powders were suspended in 5 mL HCl 0.1 N solution at 37 °C. The samples were stored 4 days in order to reach the solubility equilibrium and were periodically shaken. Posteriorly, samples were filtered through a 0.45 μm membrane filter and were quantified spectrophotometrically at 290 nm (maximum absorption wavelength of ABZ in HCl 0.1 N) (T60U spectrophotometer).

2.11. Dissolution rate of ABZ from SBA-15 and SBA-16

The rate of dissolution of ABZ from SBA-15 and SBA-16 in comparison to pure ABZ was assessed using a dissolution apparatus II under sink conditions (708-DS, Dissolution Apparatus, Agilent Technologies). A volume of 900 mL of HCl 0.1 N (pH 1.2) was used as dissolution medium at 37 °C with a paddle rotation speed of 100 rpm (Zhong et al., 2016). About 10.0 mg of pure ABZ, 33.0 mg of ABZ/SBA-15 and 78.2 mg of ABZ/SBA-16 were incorporated to each dissolution vessel. The amount of ABZ-loaded carriers was defined in order to contain about 10 mg of ABZ for comparison purposes. At defined time intervals, samples of 5 mL were taken and in order to maintain a constant volume fresh medium was added (at 37 °C) (Agilent 8000, Dissolution Sampling Station, Agilent Technologies). The ABZ concentration was measured with a UV–visible spectrophotometer at 290 nm (T60U spectrophotometer). The assays were done in triplicate and mean values are informed.

2.12. Drug release kinetic models

The ABZ and ABZ-loaded carriers release kinetics were analyzed by employing the Probit model (Tsong et al., 1997a, 1997b) (Eq. (1)), the Gompertz model (Costa et al., 2003) (Eq. (2)), the Weibull function (Langenbucher, 1972) (Eq. (3)) and the logistic function (Costa and Lobo, 2001; Tsong et al., 1997b) (Eq. (4)).

$$F = F_{max}\Phi(\alpha + \beta log t) \quad (1)$$

$$F = F_{max}e^{-\alpha e^{(-\beta log t)}} \quad (2)$$

$$F = F_{max}\left[1 - e^{-\left(\frac{t^{\beta}}{\alpha}\right)}\right] \quad (3)$$

$$F = F_{max}\left[\frac{e^{(\alpha+\beta log t)}}{1 + e^{(\alpha+\beta log t)}}\right] \quad (4)$$

where F is the fraction (%) of drug released in time t and F_{max} is the maximum fraction of the drug released at infinite time. α is the scale parameter in each model and is related to the time scale of the process. Whereas β is the acceleration or shape parameter associated with the dissolution rate per unit of time. In Eq. (1), Φ is the standard normal distribution of dissolution profile.

In Equations (2–4), the kinetic parameters were obtained after linearization while the parameters in Eq. (1) were adjusted minimizing the sum of squared errors between the experimental and drug released fractions calculated from the cumulative distribution function. Additionally, the accuracy of the obtained parameters was validated by means of the DDSolver software (Zhang et al., 2010).

The Akaike Information Criteria (AIC) was used in this study to evaluate the goodness of the release models employed to describe the dissolution profiles (Simionato et al., 2018). The AIC is defined by equation (5):

$$AIC = nln(WSSR) + 2p \quad (5)$$

where n is the number of dissolution measurements, p is the number of parameters that were adjusted in each model, WSSR *is* the weight sum of square residues. When comparing mathematical models, a smaller AIC value leads to a better fit.

3. Results and discussion

3.1. Characterization of SBA-15 and SBA-16 parent materials

3.1.1. X-ray diffraction

Fig. 1a shows the X-ray diffraction pattern of SBA-15. The XRD data showed a well resolved pattern with a prominent peak at 2θ ca. 0.9° and two peaks at 2θ ca. 1.62 and 1.8° for the synthesized sample. The corresponding d-spacings are (100) = 9.8 nm; (110) = 5.45 nm and (210) = 4.9 nm that are in accordance with values previously reported for this material (Newalkar and Katsuki, 2000). These planes are characteristic for the *P6mm* symmetry group (Fulvio et al., 2005). The unit cell dimension estimated as $a_0 = d_{100}\,(2/3^{1/2})$ has a value of 11.3 nm. X-ray diffraction pattern of SBA-16 at Fig. 1b reveals its three-dimensional cubic cage structure (*Im3m* space group). This pattern shows a very strong peak at 2θ ca. 0.78° and a small peak corresponding to 2θ ca. 1.1° in agreement with the data reported in literature (Wang et al., 2004). The corresponding d-spacings are (110) = 11.3 nm and (220) = 8.03 nm. Both reflections yield a unit cell parameter of a_0 = 16 nm confirming that the measured structure is indeed the *Im3m* SBA-16 structure. It should be noted that if the structure was hexagonal or lamellar, the shoulder would be at a completely different position. Other informed patterns of SBA-16 materials present similar unit cell parameters (Andrade et al., 2012; Grudzien et al., 2007).

3.1.2. Particles' morphology, size, and pore structure

The SEM images showed a rod-like shape for SBA-15 particles with a uniform rod length around 0.5–1.5 μm (Fig. 2a). The described morphology was in accordance with the one reported by Belmoujahid et al. (2015) (Belmoujahid et al., 2015). On the other hand, most SBA-16 particles exhibited an irregular shape (Fig. 2b) similar to the morphology found by Feliczak-guzik et al. (2016) (Feliczak-guzik et al., 2016). The maximum Feret diameter of SBA-16 particles was between 5 and 10 μm. TEM was employed to corroborate the ordered pore structure of SBA-15 and SBA-16. The microphotographs revealed that the materials were greatly porous. SBA-15 showed a mean pore size around 5 nm (measured through image analysis) and a periodical well-organized hexagonal array was detected once the electron beam was perpendicular to the main axis of the material (i.e., vertical orientation) (Fig. 2c). For parallel orientation (i.e., electron beam parallel to the main axis), a channel structure of the mesopores with parallel stripes was observed (Fig. 2d). These results verified the typical two-dimensional structure of the material (Wang et al., 2012). For SBA-16 the mean pore size was about 6 nm (measured from the images). Unidirectional pore channels were observed at vertical orientation (Fig. 2e). For the parallel orientation the usual cubic arranged and uniform pore arrays were shown (Fig. 2f) (de Oliveira Freitas et al., 2015). Therefore, TEM images verified the ordered structure of the synthesized materials.

3.1.3. FT-IR and N_2 sorption analyses of SBA-15, SBA-16 materials before and after ABZ loading

Fig. 3a exhibits FT-IR spectroscopy of pure ABZ. The absorption peak related to the stretching vibration mode of amide N-H was found at around 3323 cm^{-1}. The absorption band from the alipha-

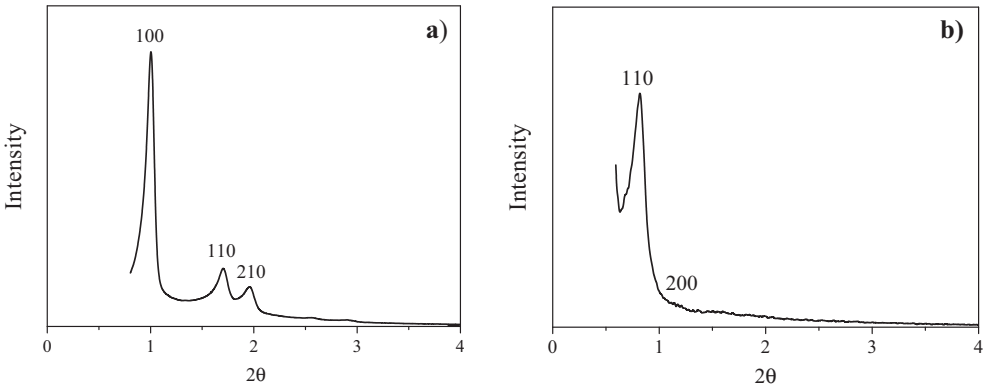

Fig. 1. XRD diffraction patterns of: (a) SBA-15 and (b) SBA-16.

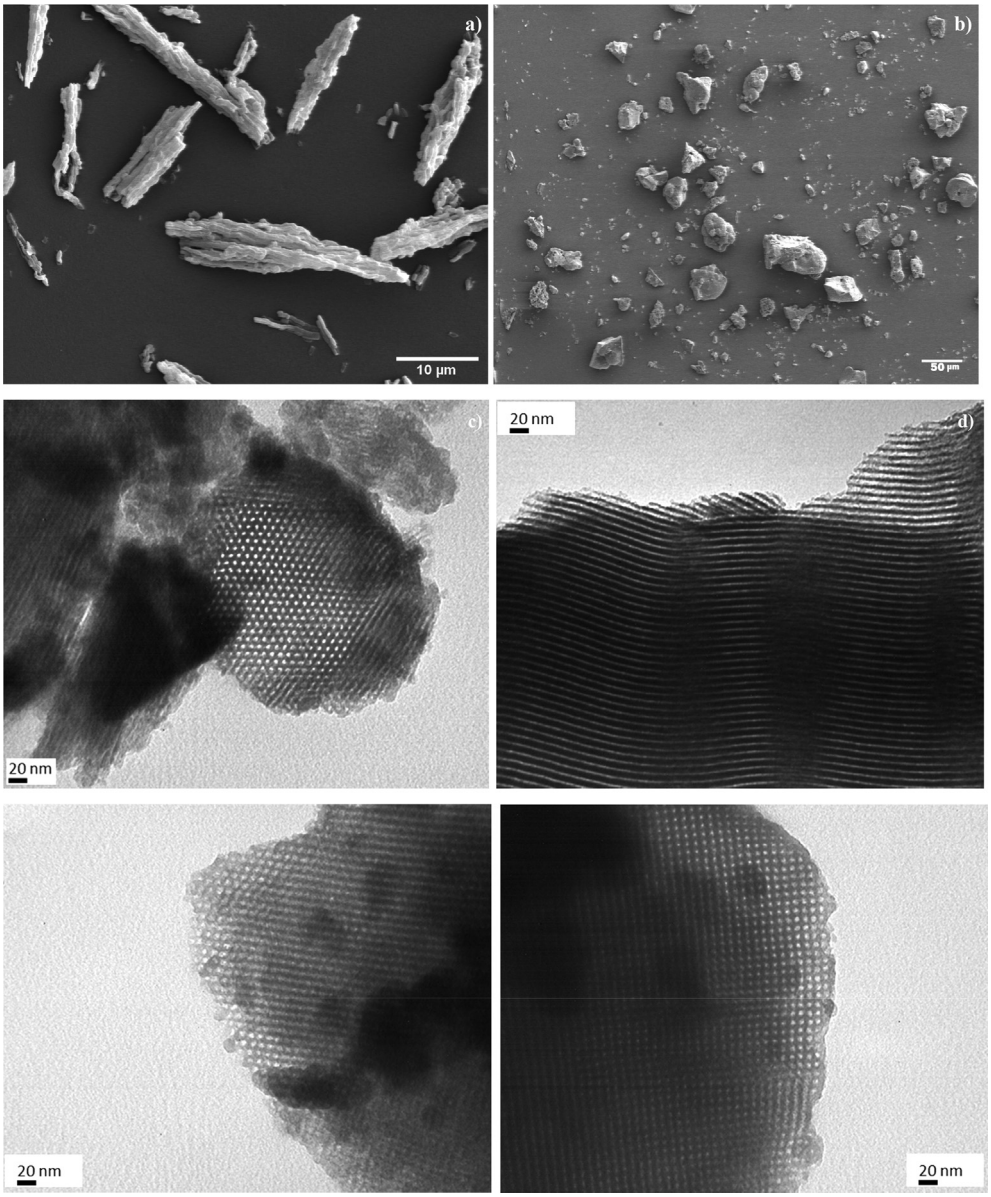

Fig. 2. SEM images: (a) SBA-15 (2000x) and (b) SBA-16 (480x). TEM images (270000x): at vertical orientation (c) SBA-15, (e) SBA-16 and at parallel orientation d) SBA-15, f) SBA-16.

tic hydrocarbon group (C-H) was observed at around 2960 cm^{-1}. The peak located at about 1713 cm^{-1} showed the ester C=O bond of the carbamate portion of the drug. The peak at around 1623 cm^{-1} presented the aromatic C=C bond, which together with the amide N-H bond represent the benzimidazole portion of the ABZ molecule. The band at around 1523 cm^{-1} showed the stretching vibration mode of the C=N group. Thus, FTIR spectroscopy revealed the usual bands of pure ABZ (Koradia et al., 2018; Tavares Cavalcanti et al., 2012). In addition, the FT-IR spectra confirmed the chemical nature of SBA-15 and SBA-16 carriers (Fig. 3b). An absorption band at around 3739 cm^{-1} presented the symmetrical stretching vibration mode of O-H bond related to silanol (Si-OH) groups. A wide intense peak at 3500–3300 cm^{-1} and a peak at around 1630 cm^{-1} were associated to the O-H bending and stretching vibration mode of the water molecules adsorbed on the material surface. The peaks situated at 1080 cm^{-1} and 800 cm^{-1} were assigned to the anti-symmetric vibrations of non-bonding oxygen atoms (Si-O) of Si-OH and symmetric stretching vibrations of Si-O-Si group, respectively. The peak corresponding to the internal vibration between Si-O-Si tetrahedral of SBA-15 and SBA-16 was observed at around 460 cm^{-1}. Also, the typical band related to the stretching vibration of Si-OH group appeared at 970 cm^{-1} (Chen et al., 2011; Ghosh et al., 2015; Giraldo et al., 2014; Zhang et al., 2016). After the drug loading, the FT-IR spectra still presented the typical band of SBA-15 and SBA-16 (at 1080 cm^{-1}) demonstrating that the surface chemistry of the materials was not modified (Fig. 3c). Moreover, the presence of ABZ in the mesoporous carriers was recognized by the FT-IR spectroscopy. For ABZ/SBA-15 several different bands related to ABZ were found at: 3323 cm^{-1}(N-H), 2960 cm^{-1}(C-H), 1713 cm^{-1}(C=O=), 1623 cm^{-1}1 (C=C) and 1523 cm^{-1} (C=N). The ABZ/SBA-16 sample also revealed the presence of ABZ in the mesoporous silica. The peak related to ABZ at 3323 cm^{-1} was not detected but the peak at 1713 cm^{-1} appeared with a similar intensity to the one presented in the spectrum of ABZ/SBA-15. The bands at around 1623 cm^{-1} and 1523 cm^{-1} presented lower intensity than the cor-

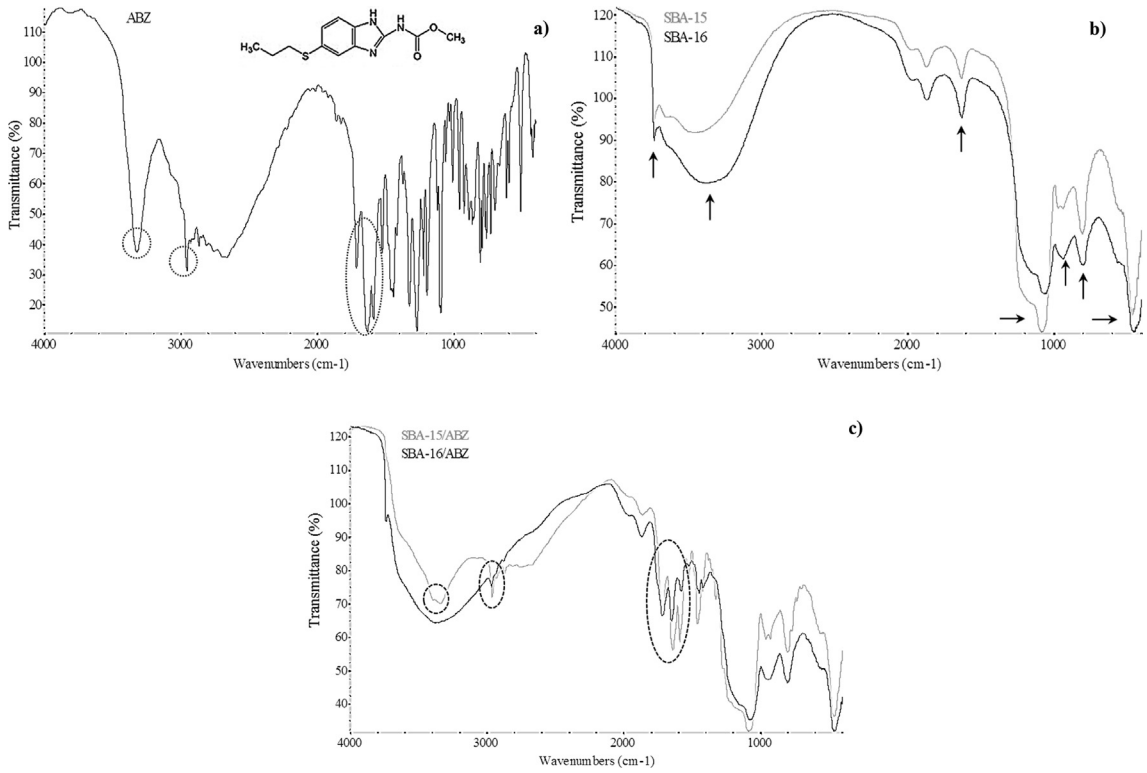

Fig. 3. FT-IR spectra of (a) ABZ, (b) SBA-15 and SBA-16, and (c) SBA-15/ABZ and SBA-16/ABZ.

responding bands observed in ABZ/SBA-15 spectrum. These results suggest that a lower percentage of ABZ was loaded in SBA-16 in comparison to SBA-15. Posteriorly, these results were confirmed by sorption isotherms and elemental analysis.

Fig. 4 presents the N_2 adsorption/desorption isotherms and pore size distributions (PSDs) for SBA-15 and ABZ/SBA-15 (Fig. 4a), and SBA-16 and ABZ/SBA-16 (Fig. 4b). Parent SBA-15 and SBA-16 materials exhibited type IV isotherms characteristic of mesoporous solids with microporous content. SBA-15 isotherm presented H1 hysteresis loop typical of mesoporous materials with one dimensional cylindrical channels opened at both sides (Gonzalez et al., 2018) (Fig. 4a). Instead, SBA-16 showed H2 hysteresis loop at the high relative pressure region characteristic of uniform cage-like mesoporous materials with interconnected pores (Fig. 4a) (Xu et al., 2007). It is important to highlight that PSDs of SBA-15 and ABZ/SBA-15 were derived from the desorption branch of nitrogen isotherm by using the BJH model. On the other hand, for SBA-16 and ABZ/SBA-16 the PSDs were obtained using the adsorption branch. This branch was selected because the cage-like pore structure presents percolation phenomenon on the desorption branch (Sapag, 2011). From the PSDs it was observed that the average pore sizes of SBA-15 and SBA-16 were 5.6 nm for both materials which is in good agreement with the TEM results.

The nitrogen sorption isotherms of both SBA-15 and SBA-16 showed a reduction in the total volume of adsorbed nitrogen after ABZ loading; indicating a significant pore filling of the mesoporous carriers (Fig. 4). In addition, SBA-15/ABZ showed a more significant reduction in the pore size than SBA-16/ABZ. Even though the surface area changed, the shape of the isotherms remained the same after drug loading, indicating that the mesoporous texture of carriers was preserved.

Table 1 presents the following textural properties of SBA-15 and SBA-16 before and after drug loading: BET surface area, total pore volume, microporous surface area and micropore volume calcu-

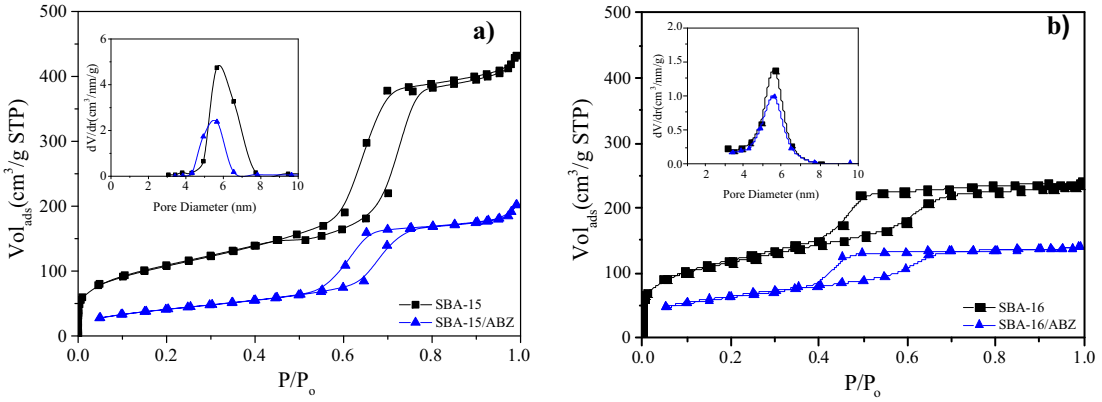

Fig. 4. Nitrogen sorption isotherms and pore size distribution (inset) of: (a) SBA-15 and ABZ/SBA-15 and (b) SBA-16 and ABZ/SBA-16.

lated using the t-plot method and the pore size using the BJH method. BET surface area of SBA-15 and SBA-16 presented similar values. However, the total pore volume of SBA-16 is significantly lower than the total pore volume of SBA-15. After drug loading, decreases in BET surface area, total pore volume, micropore surface area and micropore volume were observed. These changes can be explained by the loading of ABZ into pores of mesoporous silica. These results are in good agreement with FT-IR and N_2 sorption data indicating that the drug was loaded in the materials. Consequently, in order to quantify the amount of loaded drug in the mesoporous carriers, elemental analysis was done showing a drug loading of 30.3 wt% and 12.8 wt% for SBA-15 and SBA-16 samples, respectively.

3.2. Solubility and dissolution studies

The solubility study showed that pure crystalline ABZ had a very low solubility value of 0.0152 ± 0.0002 mg/mL in acid medium (HCl 0.1 N). Instead, ABZ loaded in the mesoporous materials presented an increment in the drug solubility in comparison to the pure ABZ: 0.0171 ± 0.0011 mg/mL and 0.0190 ± 0.0013 mg/mL for ABZ/SBA-16 and ABZ/SBA-15, respectively. These results could be related to the porous structure of the mesoporous materials, which produce a restrictive effect that did not allow the formation of the drug crystalline form. Indeed, the drug molecules were limited and stabilized inside the pores in an amorphous state (Mccarthy et al., 2015). Crystalline solids have a high crystal packing energy that is disrupted during the solubilization process. On the other hand, amorphous solids possess low packing energy and no long-range order of molecular packing. These characteristics produce that drugs in amorphous state commonly exhibits greater solubility than the crystalline solids (Kim et al., 2008; Zhong et al., 2016). The change of the ABZ structure from crystalline to amorphous state was corroborated through DSC analysis. As it can be seen in Fig. 5, the thermograms of ABZ/SBA-15 and ABZ/ SBA-16 samples did not show the typical melting endothermic peak of crystalline ABZ (at 209 °C (Tavares Cavalcanti et al., 2012)) demonstrating the amorphous state of the drug. ABZ/SBA-15 showed higher solubility than ABZ/SBA-16. Regarding these results, the two mesoporous materials presented similar surface area and pore size; hence the higher solubility of ABZ/SBA-15 may be attributed to the large total pore volume of this material in comparison to ABZ/SBA-16 (Table 1). The great volume of pores first produced a better soaking of the drug and consequently generated better contact with the medium, which leads to an increase in the solubility of the drug (Zhong et al., 2016). In Fig. 6, the dissolution profiles showed a notable increment of the release rate of the loaded drug. In particular, ABZ/SBA-15 and ABZ/SBA-16 released around 50% of the drug at 5 min of the assay in comparison to pure ABZ that only released about 1% at this point time. Notably, SBA-15 released around 98 ± 2% of the drug in 2 h, becoming a promising candidate platform to improve ABZ oral bioavailability. The higher dissolution rate of ABZ/SBA-15 in comparison to ABZ/SBA-16 could be attributed to its highest solubility as previously mentioned together with the 2D hexagonal array of the mesopores. In this sense, Porras Quevedo et al. (2017) (Porras Quevedo et al., 2017) reported a greater release rate of ibuprofen

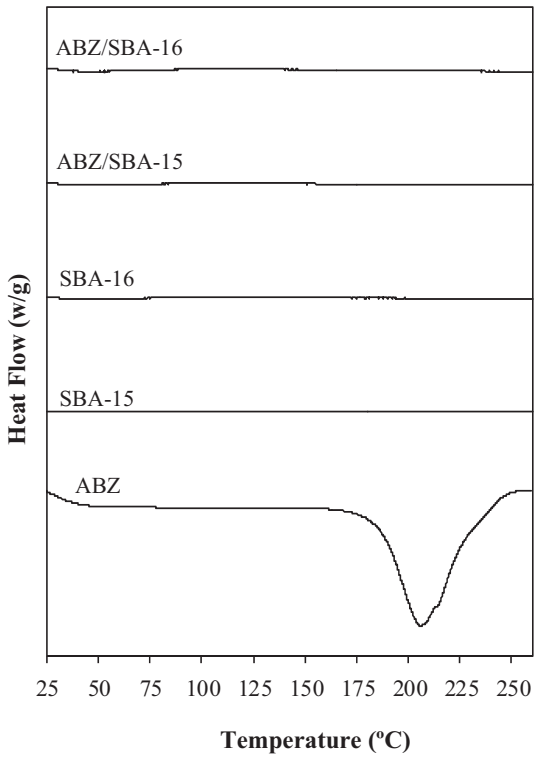

Fig. 5. DSC patterns of ABZ, SBA-15, SBA-16, ABZ/SBA-15 and ABZ/SBA-16.

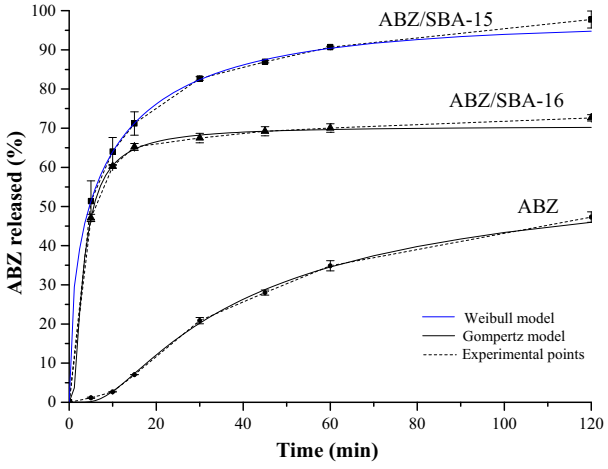

Fig. 6. Release profiles of pure ABZ, ABZ/SBA-15 and ABZ/SBA-16.

Table 1
Textural properties of SBA-15 and SBA-16 materials.

Sample	S_{BET}[a] (m^2/g)	V_t[b] (cm^3/g)	S_μ[c] (m^2/g)	V_μ[d] (cm^3/g)
SBA-15	387	0.638	31	0.013
SBA-16	409	0.361	105	0.048
ABZ/SBA-15	152	0.286	0	0.000
ABZ/SBA-16	222	0.214	27	0.011

[a] BET specific surface area.
[b] Total pore volume.
[c] Micropore surface area calculated using the *t*-plot method.
[d] Micropore volume calculated using the *t*-plot method.

Table 2
ABZ, ABZ/SBA-15 and ABZ/SBA-16 kinetics parameters according to Probit, Gompertz, Weibull and logistic models.

Model	Statistics	ABZ	ABZ/SBA-15	ABZ/SBA-16
Probit	α	−4.32	−0.76	−1.04
	β	2.83	1.04	2.14
	r^2	1.00	1.00	1.00
	AIC	11.96	1.98	8.76
Gompertz	α	25.53	1.76	3.81
	β	2.10	1.04	3.21
	r^2	1.00	1.00	1.00
	AIC	**11.44**	4.14	**6.57**
Weibull	α	639.12	3.03	3.26
	β	1.82	0.52	0.82
	r^2	1.00	1.00	1.00
	AIC	16.45	**1.19**	11.93
Logistic	α	−7.43	−1.23	−1.85
	β	4.92	1.59	3.67
	r^2	1.00	1.00	1.00
	AIC	13.04	1.85	6.93

Bold numbers correspond to the best fit.

from SBA-15 than SBA-16 due to the different morphology of the mesoporous materials.

As ABZ/SBA-15 is a promising candidate platform to improve ABZ oral bioavailability, a stability test of SBA-15 was carried out. This test was performed under the same conditions chosen for the drug loading procedure (i.e., concentrated acetic acid, 48 h at ambient temperature). The BET area of SBA-15 before and after the acidic treatment was 387 and 389 m^2/g, respectively. Therefore, these results verified that SBA-15 was unaffected by acetic acid exposure. Similar results were found by El Mourabit et al. (2012) when SBA-15 was attacked by phosphoric acid.

3.3. Release modeling

The dissolution profiles corresponding to ABZ, ABZ/SBA-15 and ABZ/SBA-16 were evaluated by fitting experimental data to the Probit, Gompertz, Weibull and logistic models. The parameters for each kinetics equation, the determination coefficient (r^2) as well as Akaike Information Criteria (AIC) values are listed in Table 2. These latter values were used to evaluate the goodness of the release models. Based on determination coefficient (r^2) as well as AIC, the Gompertz model is the function that best fit the dissolution data of ABZ and ABZ/SBA-16 while the Weibull model fits properly the dissolution data of ABZ/SBA-15. In this sense, the Gompertz model is more useful for comparing the release profiles of drugs having an intermediate release rate as ABZ and ABZ/SBA-16. This model has a sharp increment in the beginning and converges slowly to the asymptotic maximal dissolution (Lokhandwala et al., 2013). On the other hand, the Weibull model is more appropriate for comparing the release profiles of drug loaded into carriers, which significantly increase the drug dissolution rate. In Table 2, it is possible to observe that the shape parameter β of Weibull equation is higher than 1 for ABZ describing a sigmoid shape with upward curvature followed by a turning point. For ABZ/SBA-15 and ABZ/SBA-16, the shape parameter β was lower than 1 because those dissolution profiles presented an initial slope higher than the corresponding one of ABZ. After that, the dissolution profiles were consistent with an exponential function (Costa and Lobo, 2001). The models that best represent the dissolution experimental data were shown in Fig. 6 in order to demonstrate the goodness of the parameters fit.

4. Conclusions

In the present work the synthesized SBA-15 and SBA-16 presented the typical structure, morphogy and textural properties of these mesoporous materials. ABZ was effectively loaded into the mesopores of the carriers in an amorphous state resulting in a increment in the solubility. In addition, a notable increment in the dissolution rate in comparison to the pure crystalline drug was achieved. The Weibull model properly described the ABZ-SBA-15 release profile. On the other hand, the Gompertz function accurately fitted the pure ABZ and ABZ/SBA-16 dissolution profiles. The SBA-15 carrier showed the highest drug loading and dissolution rate becoming a promising plataform to enhance ABZ oral bioavailability. The ABZ/SBA-15 is a powder whose production is simple and potentially scalable. Besides, the material could be formulated in common oral pharmaceutical dosage forms as capsules. Further investigations are required to evaluate the *in-vivo* pharmacokinetic performance of ABZ/SBA-15 as a suitable alternative for the human echinococcosis treatment.

Declaration of Competing Interest

The authors declare that they have no known competing financial interests or personal relationships that could have appeared to influence the work reported in this paper.

Acknowledgments

The authors thank the financial support from Consejo Nacional de Investigaciones Científicas y Técnicas (CONICET) [grant number PIP 11220150100704CO], Agencia Nacional de Promoción Científica y Tecnológica (ANPCyT) [grant number PICT-2016-0976] and Universidad Nacional del Sur [grant number PGI 24/M138]. Authors gratefully thank Laboratório LABPEMOL (Laboratório de Peneiras Moleculares) for the X-ray diffraction analysis.

References

Abbaraju, P., 2017. Mesoporous silica nanoparticles for biomedical applications. University of Queensland.

Abulaihaiti, M., Wu, X., Qiao, L., Lv, H., Zhang, H., 2015. Efficacy of Albendazole-Chitosan Microsphere-based Treatment for Alveolar Echinococcosis in Mice 1–16. 10.1371/journal.pntd.0003950

Anadol, D., Özçelik, U., Kiper, N., Göçmen, A., 2001. Treatment of hydatid disease. Paediatr. Drugs 3, 123–135. https://doi.org/10.2165/00128072-200103020-00005.

Andrade, G.F., Cristian, D., Soares, F., Kenned, R., Almeida, D.S., Sousa, B., 2012. Mesoporous silica SBA-16 functionalized with alkoxysilane groups : preparation, characterization and release profile study. J. Nanomater. 1–10. https://doi.org/10.1155/2012/816496.

Belmoujahid, Y., Bonne, M., Scudeller, Y., Schleich, D., Grohens, Y., Lebeau, B., 2015. SBA-15 mesoporous silica as a super insulating material. Eur. Phys. J. Spec. Top. 224, 1775–1785. https://doi.org/10.1140/epjst/e2015-02498-3.

Brunetti, E., Junghanss, T., 2009. Update on cystic hydatid disease. Curr. Opin. Infect. Dis. 22, 497–502. https://doi.org/10.1097/QCO.0b013e328330331c.
Castro, S.G., Bruni, S.S., Lanusse, C.E., Allemandi, D.A., Palma, S.D., 2010. Improved albendazole dissolution rate in pluronic 188 solid dispersions. AAPS PharmSciTech 11, 1518–1525. https://doi.org/10.1208/s12249-010-9517-6.
Chattah, A.K., Pfund, L.Y., Zoppi, A., Longhi, M.R., Garnero, C., 2017. Toward novel antiparasitic formulations: complexes of Albendazole desmotropes and β-cyclodextrin. Carbohydr. Polym. 164, 379–385. https://doi.org/10.1016/j.carbpol.2017.01.098.
Chen, L., Hu, J., Qi, Z., Fang, Y., Richards, R., 2011. Gold Nanoparticles intercalated into the walls of mesoporous silica as a versatile redox catalyst. Ind. Eng. Chem. 50, 13642–13649. https://doi.org/10.1021/ie200606t.
Costa, F.O., Sousa, J.J.S., Pais, A.A.C.C., Formosinho, S.J., 2003. Comparison of dissolution profiles of Ibuprofen pellets. J. Control. Release 89, 199–212. https://doi.org/10.1016/S0168-3659(03)00033-6.
Costa, P., Lobo, M.S., 2001. Modeling and comparison of dissolution profiles. Eur. J. Pharm. Sci. 13, 123–133. https://doi.org/10.1016/S0928-0987(01)00095-1.
de Oliveira Freitas, L., Gonzalez Bravo, I., Macedo de Almeida, W.A., Barros de Sousa, E.M., 2015. Mesoporous silica materials functionalized with folic acid : preparation, characterization and release profile study with methotrexate. J Sol-Gel Sci Technol 77, 186–204. https://doi.org/10.1007/s10971-015-3844-8.
El Mourabit, S., Guillot, M., Toquer, G., Cambedouzou, J., Goettmann, F., Grandjean, A., 2012. Stability of mesoporous silica under acidic conditions. RSC Adv. 2, 10916–10924. https://doi.org/10.1039/c2ra21569a.
Elsamaligy, S., 2014. Improvement of albendazole solubility and dissolution rate by ternary solid dispersion technique. Am. J. Pharm. Heal. Res. 2, 62–78. https://doi.org/10.21276/ajphr.
Evrard, B., Chiap, P., Detullio, P., Ghalmi, F., Piel, G., Hees, T. Van, 2002. Oral bioavailability in sheep of albendazole from a suspension and from a solution containing hydroxypropyl- b -cyclodextrin. J. Control. Release 85, 45–50. https://doi.org/10.1016/S0168-3659(02)00270-5.
Falagas, M.E., Bliziotis, I.A., 2007. Albendazole for the treatment of human echinococcosis: A review of comparative clinical trials. Am. J. Med. Sci. 334, 171–179. https://doi.org/10.1097/MAJ.0b013e31814252f8.
Fattahi Masoom, M., Lari, S., Fattahi, A., Ahmadnia, N., Rajabi, M., NaderiKalat, M., 2017. Medical therapy with albendazole in human hydatid cysts of the lungs and the liver : A 13-year experience. Clin. Respir. J. 12, 1076–1083. https://doi.org/10.1111/crj.12630.
Feliczak-guzik, A., Jadach, B., Piotrowska, H., Murias, M., Lulek, J., Nowak, I., 2016. Microporous and Mesoporous Materials Synthesis and characterization of SBA-16 type mesoporous materials containing amine groups. Micropor. Mesopor. Mater. 220, 231–238. https://doi.org/10.1016/j.micromeso.2015.09.006.
Fulvio, P.F., Pikus, S., Jaroniec, M., 2005. Tailoring properties of SBA-15 materials by controlling conditions of hydrothermal synthesis. J. Materails Chem. 5049–5053. https://doi.org/10.1039/b511346f.
Galarneau, A., Rodriguez, J., Coasne, B., 2014. Validity of the t - plot method to assess microporosity in hierarchical micro/mesoporous materials. Langmuir 30, 13266–13274. https://doi.org/10.1021/la5026679.
García, A., Barrera, M.G., Piccirilli, G., Vasconi, M.D., Di Masso, R.J., Leonardi, D., Hinrichsen, L.I., Lamas, M.C., 2013a. Novel albendazole formulations given during the intestinal phase of Trichinella spiralis infection reduce effectively parasitic muscle burden in mice. Parasitol. Int. 62, 568–570. https://doi.org/10.1016/j.parint.2013.08.009.
García, A., Leonardi, D., Piccirilli, G.N., Mamprin, M., Olivieri, A.C., Lamas, M., 2013b. Spray drying formulation of albendazole microspheres by experimental design. In vitro – in vivo studies. Drug Dev. Ind. Pharm. 9045, 1–9. https://doi.org/10.3109/03639045.2013.858737.
García, A., Leonardi, D., Salazar, M.O., Lamas, M.C., 2014. Modified β-cyclodextrin inclusion complex to improve the physicochemical properties of albendazole. complete in vitro evaluation and characterization. PLoS One 9, 3–10. https://doi.org/10.1371/journal.pone.0088234.
Ghosh, B.K., Hazra, S., Naik, B., Ghosh, N.N., 2015. Preparation of Cu nanoparticle loaded SBA-15 and their excellent catalytic activity in reduction of variety of dyes. Powder Technol. 269, 371–378. https://doi.org/10.1016/j.powtec.2014.09.027.
Giraldo, L., Bastidas-barranco, M., Moreno-piraján, J.C., 2014. Vapour phase hydrogenation of phenol over rhodium on SBA-15 and SBA-16. Molecules 20594–20612. https://doi.org/10.3390/molecules191220594.
Gobin, O.C., Wan, Y., Zhao, D., Kleitz, F., Kaliaguine, S., 2007. Mesostructured silica SBA-16 with tailored intrawall porosity part 1: synthesis and characterization. J. Phys. Chem. 111, 3053–3058. https://doi.org/10.1021/jp0635765.
Gonzalez, Gema, Sagarzazu, Amaya, Cordova, Amaia, Gomes, Maria Elena, Salas, Janet, Contreras, Leglys, Noris-Suarez, Karem, Lascano, Luis, 2018. Comparative study of two silica mesoporous materials (SBA-16 and SBA-15) modified with a hydroxyapatite layer for clindamycin controlled delivery. Micropor. Mesopor. Mater. 256, 251–265. https://doi.org/10.1016/j.micromeso.2017.07.021.
Grudzien, R.M., Grabicka, B.E., Jaroniec, M., 2007. Adsorption studies of thermal stability of SBA-16 mesoporous silicas. Appl Surf Sci 253, 5660–5665. https://doi.org/10.1016/j.apsusc.2006.12.033.
Haitao, L., Tao, S., Yingmei, S., Tuergan, A., Ayifuhan, A., Hao, W., 2016. Comparative evaluation of liposomal albendazole and tablet-albendazole against hepatic cystic echinococcosis. Medicine (Baltimore) 95, 1–6. https://doi.org/10.1097/md.0000000000002237.
Hu, Y., Wang, J., Zhi, Z., Jiang, T., Wang, S., 2011. Facile synthesis of 3D cubic mesoporous silica microspheres with a controllable pore size and their application for improved delivery of a water-insoluble drug. J. Coll. Interf. Sci. 363, 410–417. https://doi.org/10.1016/j.jcis.2011.07.022.
Hu, Y., Zhi, Z., Zhao, Q., Wu, C., Zhao, P., Jiang, H., Jiang, T., Wang, S., 2012. 3D cubic mesoporous silica microsphere as a carrier for poorly soluble drug carvedilol. Micropor. Mesopor. Mater. 147, 94–101. https://doi.org/10.1016/j.micromeso.2011.06.001.
Ibrahim, M.A., Al-Anazi, F.K., 2013. Enhancement of the dissolution of albendazole from pellets using MTR technique. Saudi Pharm. J. 21, 215–223. https://doi.org/10.1016/j.jsps.2012.03.001.
Ibrahim, M.A., Shazly, G.A., El-Badry, M., 2014. Albendazole microparticles prepared by spray drying technique: Improvement of drug dissolution. Trop. J. Pharm. Res. 13, 1963–1970. https://doi.org/10.4314/tjpr.v13i12.2.
Jambhrunkar, S., Yu, M., Yang, J., Zhang, J., Shrotri, A., Endo-Munoz, L., Moreau, J., Lu, G., Yu, C., 2013. Stepwise pore size reduction of ordered nanoporous silica materials at angstrom precision. J. Am. Chem. Soc. 135, 8444–8447. https://doi.org/10.1021/ja402463h.
de los Santos, C.J., Pérez-Martínez, J.I., Gómez-Pantoja, M.E., Moyano, J.R., 2017. Enhancement of albendazole dissolution properties using solid dispersions with Gelucire 50/13 and PEG 15000. J. Drug Deliv. Sci. Technol. 42, 261–272. https://doi.org/10.1016/j.jddst.2017.03.030.
Kim, J., Kim, M., Park, H.J., Jin, S., Lee, S., Hwang, S., 2008. Physicochemical properties and oral bioavailability of amorphous atorvastatin hemi-calcium using spray-drying and SAS process. Int. J. Pharm. 359, 211–219. https://doi.org/10.1016/j.ijpharm.2008.04.006.
Kohri, N., Yamayoshi, Y., Xin, H., Iseki, K., Sato, N., Todo, S., Miyazaki, K., 1999. Improving the oral bioavailability of albendazole in rabbits by the solid dispersion technique. J. Pharm. Pharmacol. 51, 159–164. https://doi.org/10.1211/0022357991772277.
Koradia, K.D., Parikh, R.H., Koradia, H.D., 2018. Journal of drug delivery science and technology albendazole nanocrystals : optimization, spectroscopic, thermal and anthelmintic studies. J. Drug Deliv. Sci. Technol. 43, 369–378. https://doi.org/10.1016/j.jddst.2017.11.003.
Langenbucher, F., 1972. Letters to the Editor: Linearization of dissolution rate curves by the Weibull distribution. J. Pharm. Pharmacol. 24, 979–981. https://doi.org/10.1111/j.2042-7158.1972.tb08930.x.
Li, H., Song, T., Qin, Y., Liu, W., Li, X., Shao, Y., Wen, H., 2015. Efficiency of liposomal albendazole for the treatment of the patients with complex alveolar echinococcosis: a comparative analysis of CEUS, CT, and PET/CT. Parasitol. Res. 114, 4175–4180. https://doi.org/10.1007/s00436-015-4649-y.
Li, Z., Barnes, J., Bosoy, A., Stoddart, F., Zink, J., 2012. Mesoporous silica nanoparticles in biomedical applications. Chem. Soc. Rev. 41, 2590–2605. https://doi.org/10.1039/c1cs15246g.
Lokhandwala, H., Deshpande, A., Deshpande, S., 2013. Kinetic modeling and dissolution profiles comparison: an overview. Int. J. Pharma Bio Sci. 4, 728–737. https://doi.org/10.22376/ijpbs.
Lu, J., Liong, M., Zink, J.I., Tamanoi, F., 2007. Mesoporous silica nanoparticles as a delivery system for hydrophobic anticancer drugs. Small 3, 1341–1346. https://doi.org/10.1002/smll.200700005.
Ma, D., Hettiarachchi, G., Nguyen, D., Zhang, B., Wittenberg, J.B., Zavalij, P.Y., Briken, V., Isaacs, L., 2012. Acyclic cucurbit[n]uril molecular containers enhance the solubility and bioactivity of poorly soluble pharmaceuticals. Nat. Chem. 4, 503–510. https://doi.org/10.1038/nchem.1326.
Martinez-Marcos, L., Lamprou, D.A., McBurney, R.T., Halbert, G.W., 2016. A novel hot-melt extrusion formulation of albendazole for increasing dissolution properties. Int. J. Pharm. 499, 175–185. https://doi.org/10.1016/j.ijpharm.2016.01.006.
Mccarthy, C.A., Ahern, R.J., Dontireddy, R., Ryan, K.B., Mccarthy, C.A., Ahern, R.J., Dontireddy, R., 2015. Mesoporous silica formulation strategies for drug dissolution enhancement : a review. Expert Opin. Drug Deliv. 13, 93–108. https://doi.org/10.1517/17425247.2016.1100165.
Movahedi, F., Li, L., Gu, W., Xu, Z.P., 2017. Nanoformulations of albendazole as effective anticancer and antiparasite agents. Nanomedicine 12, 2555–2575. https://doi.org/10.2217/nnm-2017-0102.
Newalkar, B.L., Katsuki, H., 2000. Rapid synthesis of mesoporous SBA-15 molecular sieve by a microwave – hydrothermal process. Chem. Commun. 3, 2389–2390. https://doi.org/10.1039/b007441l.
Palomares-Alonso, F., Rivas, C., Bernad-Bernad, M.J., Castillo Montiel, M., Palencia, G., González-Hernández, I., Castro-Torres, N., Pinzón Estrada, E., Jung-Cook, H., 2010. Acta Tropica Two novel ternary albendazole – cyclodextrin – polymer systems : dissolution, bioavailability and efficacy against Taenia crassiceps cysts. Acta Trop. 113, 56–60. https://doi.org/10.1016/j.actatropica.2009.09.006.
Panja, S., Dey, G., Bharti, R., Kumari, K., Maiti, T.K., Mandal, M., Chattopadhyay, S., 2016a. Tailor-made temperature-sensitive micelle for targeted and on-demand release of anticancer drugs. ACS Appl. Mater. Interfaces 8, 12063–12074. https://doi.org/10.1021/acsami.6b03820.
Panja, Sudipta, Dey, G., Bharti, R., Mandal, P., Mandal, M., Chattopadhyay, S., 2016b. Metal ion ornamented ultrafast light-sensitive nanogel for potential in vivo cancer therapy. Chem. Mater. 28, 8598–8610. https://doi.org/10.1021/acs.chemmater.6b03440.
Panja, S., Maji, S., Maiti, T.K., Chattopadhyay, S., 2015. A smart magnetically active nanovehicle for on-demand targeted drug delivery: where van der waals force balances the magnetic interaction. ACS Appl. Mater. Interf. 7, 24229–24241. https://doi.org/10.1021/acsami.5b07706.
Panwar, P., Pandey, B., Lakhera, P., Singh, K., 2010. Preparation, characterization, and in vitro release study of albendazole-encapsulated nanosize liposomes. Int. J. Nanomed. 5, 101–108. https://doi.org/10.2147/IJN.S8030.

Paredes, A.J., Llabot, J.M., Sánchez Bruni, S., Allemandi, D., Palma, S.D., 2016. Self-dispersible nanocrystals of albendazole produced by high pressure homogenization and spray-drying. Drug Dev. Ind. Pharm. 42, 1564–1570. https://doi.org/10.3109/03639045.2016.1151036.

Pensel, P.E., Castro, S., Allemandi, D., Bruni, S.S., Palma, S.D., Elissondo, M.C., 2014. Enhanced chemoprophylactic and clinical efficacy of albendazole formulated as solid dispersions in experimental cystic echinococcosis. Vet. Parasitol. 203, 80–86. https://doi.org/10.1016/j.vetpar.2014.01.027.

Pensel, P.E., Ullio Gamboa, G., Fabbri, J., Ceballos, L., Sanchez Bruni, S., Alvarez, L.I., Allemandi, D., Benoit, J.P., Palma, S.D., Elissondo, M.C., 2015. Cystic echinococcosis therapy: Albendazole-loaded lipid nanocapsules enhance the oral bioavailability and efficacy in experimentally infected mice. Acta Trop. 152, 185–194. https://doi.org/10.1016/j.actatropica.2015.09.016.

Porras Quevedo, G., Celis, A.C., Ordonez, C.V., Martinez, M.L.O., 2017. SBA-type mesoporous materials with cylindrical and spherical structures for the controlled loading and release of ibuprofen. J. Sol-Gel Sci. Technol. 85, 486–494. https://doi.org/10.1007/s10971-017-4560-3.

Priotti, J., Codina, A.V., Leonardi, D., Vasconi, M.D., Hinrichsen, L.I., Lamas, M.C., 2017. Albendazole microcrystal formulations based on chitosan and cellulose derivatives: physicochemical characterization and in vitro parasiticidal activity in trichinella spiralis adult worms. AAPS PharmSciTech 18, 947–956. https://doi.org/10.1208/s12249-016-0659-z.

Riikonen, J., Xu, W., Lehto, V.P., 2018. Mesoporous systems for poorly soluble drugs – recent trends. Int. J. Pharm. 536, 178–186. https://doi.org/10.1016/j.ijpharm.2017.11.054.

Sapag, K., 2011. Improvement in the pore size distribution for ordered mesoporous materials with cylindrical and spherical pores using the Kelvin Equation. Top Catal 54 (1-4), 121–134. https://doi.org/10.1007/s11244-011-9631-z.

Simionato, L.D., Petrone, L., Baldut, M., Bonafede, S.L., Segall, A.I., 2018. Comparison between the dissolution profiles of nine meloxicam tablet brands commercially available in Buenos Aires. Argentina. Saudi Pharm. J. 26, 578–584. https://doi.org/10.1016/j.jsps.2018.01.015.

Souza, M.C. De, Marchetti, J.M., 2012. Development of albendazole sulfoxide-loaded Eudragit microparticles: A potential strategy to improve the drug bioavailability. Adv. Powder Technol. 23, 801–807. https://doi.org/10.1016/j.apt.2011.10.009.

Stamatakos, M., Sargedi, C., Stefanaki, C., Safioleas, C., Matthaiopoulou, I., Safioleas, M., 2009. Anthelminthic treatment: An adjuvant therapeutic strategy against Echinococcus granulosus. Parasitol. Int. 58, 115–120. https://doi.org/10.1016/j.parint.2009.01.002.

Stevens, W.J.J., Lebeau, K., Mertens, M., Van Tendeloo, G., Cool, P., Vansant, E.F., 2006. Investigation of the morphology of the mesoporous SBA-16 and SBA-15 materials. J. Phys. Chem. B 110, 9183–9187. https://doi.org/10.1021/jp0548725.

Tavares Cavalcanti, N., Damasceno Sousa, G., Maciel Tabosa, M.A., Soares Sobrinho, L., Bastos Leal, L., Pereira de Santana, D., 2012. Assay and physicochemical characterization of the antiparasitic albendazole. Brazilian J. Pharm. Sci. 48, 281–290. https://doi.org/10.1590/S1984-82502012000200012.

Thakur, A., Thipparaboina, R., Kumar, D., Gouthami, K., Shatri, N., 2015. Crystal Engineered albendazole with improved dissolution and material attributes. Cryst. Eng. Comm. 1–3. https://doi.org/10.1039/C5CE02306H.

Thomas, M.J.K., Slipper, I., Walunj, A., Jain, A., Favretto, M.E., Kallinteri, P., Douroumis, D., 2010. Inclusion of poorly soluble drugs in highly ordered mesoporous silica nanoparticles. Int. J. Pharm. 387, 272–277. https://doi.org/10.1016/j.ijpharm.2009.12.023.

Tsong, Y., Hammerstrom, T., Chen, J.J., 1997a. Multipoint dissolution specification and acceptance sampling rule based on profile modeling and principal component analysis. J. Biopharm. Stat. 7, 423–439. https://doi.org/10.1080/10543409708835198.

Tsong, Y., Sathe, P.M., Shah, V.P., 1997b. In vitro dissolution profile comparison. Adv Exp Med Biol 423, 31–42.

Vogt, M., Kunath, K., Dressman, J.B., 2008. Dissolution improvement of four poorly water soluble drugs by cogrinding with commonly used excipients. Eur. J. Pharm. Biopharm. 68, 330–337. https://doi.org/10.1016/j.ejpb.2007.05.009.

Wang, L., Fan, J., Tian, B., Yang, H., Yu, C., Tu, B., Zhao, D., 2004. Synthesis and characterization of small pore thick-walled SBA-16 templated by oligomeric surfactant with ultra-long hydrophilic chains. Micropor. Mesopor. Mater. 67, 135–141. https://doi.org/10.1016/j.micromeso.2003.10.015.

Wang, Z., Chen, B., Quan, G., Li, F., Wu, Q., Dian, L., Dong, Y., Li, G., Wu, C., 2012. Increasing the oral bioavailability of poorly water- soluble carbamazepine using immediate-release pellets supported on SBA-15 mesoporous silica. Int. J. Nanomedicine 7, 5807–5818. https://doi.org/10.2147/IJN.S37650.

WHO, 2019. Echinococcosis [WWW Document]. World Heal. Organ. URL (accessed 5.24.19). https://www.who.int/news-room/fact-sheets/detail/echinococcosis.

Xu, R., Pang, W., Yu, J., Huo, Q., Chen, J., 2007. Chemistry of zeolites and related porous materials : synthesis and structure. Wiley-VCH Verlag GmbH & Co..

Xu, W., Riikonen, J., Lehto, V.P., 2013. Mesoporous systems for poorly soluble drugs. Int. J. Pharm. 453, 181–197. https://doi.org/10.1016/j.ijpharm.2012.09.008.

Zhang, X., Cresswell, M., 2016. Inorganic controlled release technology: materials and concepts for advanced drug formulation. Inorganic Controlled Release Technology. Butterworth-Heinemann.

Zhang, X., Yang, H., Huo, Y., Li, J., Ma, Jianxin, Ma, Jiantai, 2016. Cu(I)-Functionalized SBA-16: an efficient catalyst for the synthesis of α-ketoamides under moderate conditions. Dalt. Trans. 45, 8972–8983. https://doi.org/10.1039/c5dt04969e.

Zhang, Y., Huo, M., Zhou, J., Zou, A., Li, W., Yao, C., Xie, S., 2010. DDSolver: An add-in program for modeling and comparison of drug dissolution profiles. AAPS J. 12, 263–271. https://doi.org/10.1208/s12248-010-9185-1.

Zhao, D., Zhao, D., Feng, J., Huo, Q., Melosh, N., Fredrickson, G.H., Chmelka, B.F., Stucky, G.D., 1998. Triblock copolymer syntheses of mesoporous silica with periodic 50 to 300 angstrom pores. Science (80-.) 279, 548–552. https://doi.org/10.1126/science.279.5350.548.

Zhong, S., Huang, W., Tian, Y., Wang, X., 2016. Synthesis of mesoporous carbon spheres and release of albendazole. Mater. Lett. 179, 86–89. https://doi.org/10.1016/j.matlet.2016.05.036.